In situ Structural Study of Sb(V) Adsorption on Hematite (1-102) Using X-ray Surface Scattering

Qiu, C.; Majs, F.; Douglas, T.; Schmidt, M.; Trainor, T.;

Originally published:

September 2018

Environmental Science & Technology 52(2018)19, 11161-11168

DOI: https://doi.org/10.1021/acs.est.8b03903

In situ Structural Study of Sb(V) Adsorption on Hematite ($1\bar{1}02$) Using X-ray Surface Scattering

Canrong Qiu[a, *], Frantisek Majs[a, 1], Thomas A. Douglas[b], Moritz Schmidt[c], Thomas P. Trainor[a]

[a] *Department of Chemistry and Biochemistry, University of Alaska Fairbanks, Fairbanks, Alaska, USA*

[b] *U.S. Army Cold Regions Research and Engineering Laboratory, Fort Wainwright, Alaska, USA*

[c] *Helmholtz-Zentrum Dresden-Rossendorf, Institute of Resource Ecology, Dresden, Germany*

Abstract

The binding mechanism of Sb(V) on a single crystal hematite ($1\bar{1}02$) surface was studied using crystal truncation rod X-ray diffraction (CTR) under in situ conditions. The best fit CTR model indicates Sb(V) adsorbs at the surface as an inner-sphere complex forming a tridentate binding geometry with the nearest Sb-Fe distance of 3.09(4) Å and an average Sb-O bond length of 2.08(5) Å. In this binding geometry Sb is bound at both edge-sharing and corner-sharing sites of the surface Fe-O octahedral units. The chemical plausibility of the proposed structure was further verified by bond valence analysis, which also deduced a protonation scheme for surface O groups. The stoichiometry of the surface reaction predicts the release of one OH^- group at pH 5.5.

1. Introduction

Recent concerns over antimony (Sb) contamination and potential toxicity have resulted in increased attention to the chemistry of this element in aquatic and soil environments. Antimony is widely used in commercial products, including as a fire retardant, a catalyst in plastic manufacturing, a lubricant in automobile brake linings, and as a hardener in Pb-alloy used for the manufacture of lead-acid batteries and ammunition.[1, 2] Release of Sb into the environment,

* Corresponding author. Present address: Helmholtz-Zentrum Dresden-Rossendorf, Institute of Resource Ecology, Dresden, Germany. Tel. : +4903512603154

E-mail address: c.qiu@hzdr.de (C. Qiu)

[1] Current address: Agriculture Department, Stephen F. Austin State University, Nacogdoches, Texas, USA

whether unintentional or intentional like in the case of spent ammunition at shooting ranges,[3, 4] represents a potential risk to human health. Concerns associated with elevated Sb in the environment are due to its toxicity and its potential to cause respiratory irritation, pneumoconiosis, antimony spots on the skin and gastrointestinal symptoms.[5] Furthermore, antimony trioxide (Sb_2O_3) is classified as potentially carcinogenic (Group 2B) to humans by the International Agency for Research on Cancer.[6] Although Sb has some therapeutic uses for the treatment of leishmaniasis and schistosomiasis,[7] it has been found to cause serious side effects such as cardiotoxicity and pancreatitis.[8, 9] The United States Environmental Protection Agency has added Sb to the list of priority contaminants and set the maximum contamination level of Sb in drinking water at 6 μg L^{-1}.[10] The evaluation of environmental risks posed by Sb necessitates the knowledge of its environmental behavior, such as its speciation and dispersion in soils and ground water, which are mainly determined by the associated retention mechanisms and interactions with different minerals in the environment.

Antimony is typically found in three oxidation states, including Sb(0), Sb(III), and Sb(V). Elemental Sb is readily oxidized to Sb(III) (within minutes) under ambient environmental conditions. Further oxidation of Sb(III) to Sb(V) is kinetically controlled with a time scale of >10 hours depending on the aqueous composition.[11] Numerous studies of Sb(III) binding mechanisms on the surfaces of natural sorbents, such as pyrite and goethite, suggest surface adsorption can greatly facilitate Sb(III) oxidation.[12-14] While Sb(III) is found to be prevalent within some reducing aqueous systems,[15] the facile oxidation of Sb(III) in the natural environment results in Sb speciation being dominated by Sb(V).[16]

Adsorption of Sb(V) on natural substrates, such as Fe/Al-(oxyhydr)oxides, is among the primary mechanisms controlling the environmental fate and dispersion of Sb in soil and aquatic settings.[17, 18] A number of recent studies have focused on elucidating Sb adsorption, including batch adsorption experiments,[12, 19, 20] X-ray spectroscopy (XAFS)[4, 17, 21, 22] and theoretical methods.[23, 24] Batch adsorption experiments coupled with surface complexation modeling methods suggest Sb(V) adsorption to Fe-(oxyhydr)oxides is mainly via an inner-sphere binding mode with different binding geometries depending on the substrate types. For example, Sb(V) sorption to goethite was explained via a mononuclear bidentate binding mode.[12, 19] This was in contrast to a different iron-oxide-rich soil sample, where Sb(V) was found to adsorb at the substrate surface with a bidentate binding structure.[25] Interestingly, Sb(V) sorption to in-lab

synthesized iron-oxide-coated sands was found to occur with both inner-sphere and outer-sphere binding modes.[20]

Consistent with results from batch adsorption studies, XAFS studies also suggest inner-sphere binding configurations with further structural details that identify two types of inner-sphere species corresponding to Sb-Fe separations of ~ 3.1 Å and ~ 3.5 Å, respectively.[3, 4, 17, 22, 26] The shorter of the two Sb-Fe was assigned to a bidentate edge-sharing binding mode, while the longer Sb-Fe distance (~ 3.5 Å) was attributed to a bidentate corner-sharing binding configuration. Results from XAFS studies also suggest the substrate type plays a key role in determining the binding structure. Synthetic iron (hydr)oxide samples, such as hydrous ferric oxide,[22] goethite,[17] and ferrihydrite[17] exhibit Sb(V) binding through an edge-sharing mode while less ordered iron (hydr)oxide samples, such as ferrihydrite,[17] also show affinity for Sb(V) binding through a corner-sharing mode. A similar coexistence of two binding geometries was reported for shooting range soils[3, 4] and sediment samples close to a Sb mining site.[26] The heterogeneity of Sb(V) adsorption modes on Fe-(oxyhydr)oxide surfaces was also implied in a desorption test, where different desorption rates of Sb(V) from amorphous iron oxide samples were observed.[27] These results all suggest an inner-sphere binding mode; however, they do not provide a consensus on the binding geometry or identify any impact surface structure may have on the binding configuration.

To accurately determine the surface binding structure of compounds with XAFS measurements, the surface structure of the substrate must be well characterized. This is typically difficult when using powder samples. For example, while XAFS provides direct structural information of metal(loid) binding there is potential for ambiguity in describing sorbate binding sites when it is in the presence of multiple reactive surface sites on the substrate.[28, 29] In the context of multiple potential binding configurations as suggested in the aforementioned XAFS studies,[4, 17, 21, 22] the nature of Sb binding on mineral surfaces cannot be fully understood without knowing the detailed structure of the surface. Therefore, studies of sorption to well-characterized mineral surfaces can be used to reduce the ambiguity in identifying binding sites and geometries.

To better quantify Sb binding to hematite, we used crystal truncation rod X-ray diffraction (CTR) to characterize Sb(V) adsorption on a single crystal hematite $(1\bar{1}02)$ surface. CTR probes long-range structural ordering at a single crystal surface with high sensitivity.[30] The method allows the determination of preferred binding site(s) and the associated binding modes for

aqueous ions, which provides a detailed structural interpretation of sorption reactions. The hydrated hematite ($1\bar{1}02$) surface has been extensively studied using both CTR diffraction and theoretical methods[31-35] and thus serves as an ideal model substrate to examine structure-reactivity relationships on Fe-oxides surfaces. The surface binding structure proposed in this work based on a single crystal system, adds to our understanding of the molecular interactions of Sb(V) with minerals in the environment. This will be useful for developing remediation efforts, and, if the species can be incorporated into thermodynamic models, for predicting Sb(V)'s fate in the environment.

2. Methods and experiments

2.1 Sample preparation

A natural single crystal hematite sample was first cut into a round shape with a diameter of ~ 1 cm and a thickness of ~ 0.2 cm and was then oriented within 0.1° parallel to the ($1\bar{1}02$) plane using a custom orientation and polishing jig. The oriented sample surface was ground and polished using successively smaller sizes of diamond paste down to 0.25 µm. Single crystal samples were further polished following chemical mechanical polishing (CMP) procedures described elsewhere.[32] Antimonate solutions (200 µM) were prepared inside a 4% H_2/96% N_2 filled glove box to avoid the influence of CO_2. Potassium hexahydroxyantimonate ($KSb(OH)_6$) was dissolved in deionized water, which was degassed in advance by boiling and sparging with N_2 (>99.999% pure) for 2 hours. The solution pH was carefully adjusted to pH 5.5(±0.1) using HCl and NaOH. At pH 5.5, we ensure the dominant Sb(V) species existing as $Sb(OH)_6^-$ in solution (> 99%) and a positively charged hematite surface (p.z.c. at pH 8-9 [36, 37]) to facilitate Sb(V) surface binding reactions. The Sb(V) solutions were stored inside the glove box prior to CTR measurements. The CMP-prepared hematite surface was reacted with Sb(V) solutions *in situ* using a liquid cell designed for surface diffraction measurements.[38] The sample cell used a Kapton membrane to confine a liquid film with a thickness of several µm that was maintained for the duration of the CTR measurement. To avoid dehydration of the liquid film due to diffusion of water vapor through the Kapton film, the liquid cell was capped with an additional Kapton dome with water-saturated He (relative humidity >90%) flowing through the dome headspace.

2.2 CTR Measurements

CTR measurements were conducted at the GSECARS bending magnet beamline 13BMC at the Advanced Photon Source (APS), Argonne National Laboratory, Argonne, Illinois. The energy of the incoming X-ray beam was fixed at 13 keV and the beam was focused to 0.25 × 0.44 mm. A Kappa geometry Newport diffractometer (4S+2D) was used for sample and detector orientation with angles and diffractometer coordinates defined according to You.[39] Intensity of scattered X-rays was measured using a Dectris PILATUS 100K 2D pixel array detector with 195×487 pixels (vertical × horizontal).[40] Nine CTRs (specular rod and eight non-specular rods) were collected to probe electron density in lateral and vertical dimensions. Non-specular CTR data were collected with the incident angle of the beam fixed at 2° relative to the sample surface. And the specular rod was measured with the the sample surface normal being constrained to lie in the lab-frame horizontal plane. We verified that there was no beam-induced change of the sample surface by repeating the collection of a CTR segment several times during the measurements. Repeat measurements over a defined region of (2 0 L) rod (L = 0.6–2) showed no change in intensities within experimental errors throughout the course of data collection.

2.3 CTR modeling

2.3.1 Data analysis

The full CTR dataset consisted of 1227 unique data points. The structure factor (magnitude) of each data point was extracted from each PILATUS image using the TDL software package (http://github.com/xraypy/tdl). Each data point was subject to background subtraction followed by corrections for active area, polarization, and Lorentz factors to account for the variance of the intercept between Ewald-sphere and the CTR as a function of Q using a method according to Schlepütz et al.[41]

2.3.2 Hematite $(1\bar{1}02)$ structure and terminations

The crystal structure of hematite (α-Fe_2O_3) belongs to the $R\bar{3}c$ space group and can be defined in terms of a hexagonal close packing of oxygen with iron occupying two-thirds of the octahedral holes. The lattice parameters of α-Fe_2O_3 (5.035Å, 13.747 Å, 90°, 90°, 120°) as well as the bulk isotropic Debye-Waller factors have been previously reported. [42] For convenience, the hematite $(1\bar{1}02)$ surface was re-indexed by defining a pseudo unit cell (5.035 Å, 5.427 Å, 7.364

Å, 90°, 90°, 90°) that contains the new c-axis ($\mathbf{c_s}$) normal to the surface and the a- ($\mathbf{a_s}$) and b- ($\mathbf{b_s}$) axes in-plane following the method defined by Trainor et al.[38] The re-indexed unit cell contains ten atom layers with a stoichiometric sequence of (**O_2-Fe_2-O_2-Fe_2-O_2-O_2-Fe_2-O_2-Fe_2-O_2-R**) along the $\mathbf{c_s}$ axis, where **R** is the stoichiometric repeating sequence (Fe_2O_3) in the bulk structure.

Both experimental and theoretical approaches have provided a consensus on the surface terminations of hematite ($1\bar{1}02$).[32-35] It was found that the stoichiometric sequence would dominate when the crystal sample is prepared under thermal annealing conditions.[34] However, when hydroxylated this surface, termed here the full layer termination (FLT), would bear singly coordinated oxygen ^{I}O and triply coordinated oxygen ^{III}O.[34] It has been observed in several studies that CMP sample preparation results in a mixed surface termination that is typically dominated (~80%) by the so-called half layer termination (HLT).[32, 43] The HLT displays a sequence (**O_2-X-O_2-Fe_2-O_2-O_2-Fe_2-O_2-Fe_2-O_2-R)** that has a missing near surface Fe-layer (**X**). As displayed in Fig. S2, due to the vacancy of the near-surface Fe layer, the HLT of hydroxylated hematite ($1\bar{1}02$) surface bears doubly coordinated oxygen ^{II}O in addition to singly coordinated oxygen ^{I}O and triply coordinated oxygen ^{III}O, which are also present in the FLT surface.

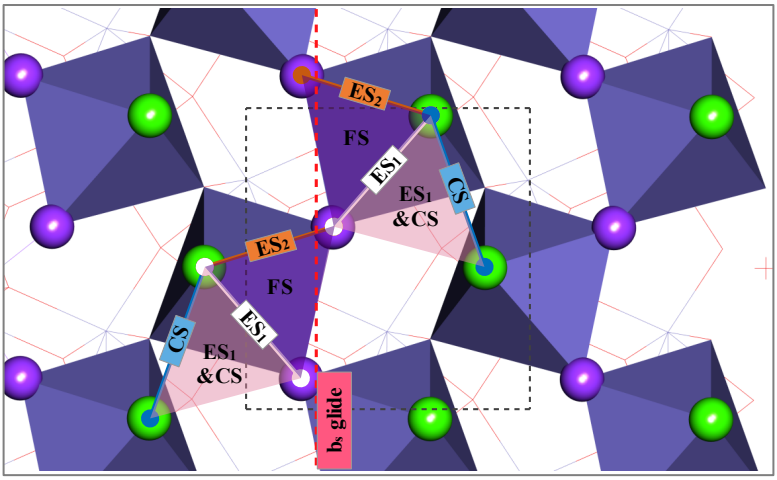

Figure 1. Potential surface binding sites on the half layer termination (HLT) of hematite ($1\bar{1}02$) including bidentate corner-sharing sites (CS), bidentate edge-sharing sites (ES_1 and ES_2), tridentate face-sharing sites (FS), and tridentate corner-sharing/edge-sharing sites (ES_1&CS). One surface unit cell is outlined by black dashed lines. Each type of site has a symmetry copy based on $\mathbf{b_s}$ glide plane symmetry highlighted as red dashed line. Terminal ^{I}O groups are

displayed as green spheres, ^{II}O atoms are displayed as purple spheres, near-surface Fe atoms are displayed as octahedra, and all the other atoms are shown as solid lines for better visual clarity.

2.3.3 Potential binding sites

With the surface functional groups identified potential surface sites for Sb adsorption on the HLT surface could be deduced (Fig. 1). When considering possible binding sites on the HLT we ignored the monodentate binding mode since it would result in a large Fe-Sb distance (>3.8 Å), that was not observed in previous XAFS studies.[4, 17, 22] In addition, Sb(V) adsorption in an octahedral coordination shell at the available bidentate edge-sharing sites (ES_1 and ES_2 in Fig. 1) were ignored, since it would lead to sterically unfavorable configuration with abnormally small O-O separations (<2.0 Å) between the 'distal' oxygens (bonding only to Sb) and the surface oxygens. As a result, the Sb binding configuration on the HLT surface was examined by comparing three trial models; bidentate corner-sharing (Model CS), tridentate corner-sharing/edge-sharing (Model CS&ES) and tridentate face-sharing (Model FS) configurations (Fig. 1). Besides the HLT, the FLT represents another type of surface domain on a CMP-prepared surface that occupies only ~20% of the substrate surface.[32] The FLT domain contribution to the overall structure factors is minor, and incorporation of sorbates within this domain are poorly constrained due to the small contribution. Therefore, we ignore surface Sb species on the FLT, and account for the presence of this surface using an average structure model, which displays as a HLT-like structure but with the top three atomic layers bearing partial occupancy to account for the coexistence of the FLT.

2.3.4 CTR model refinement

The CTR structure factor calculation has been described in detail elsewhere.[30, 44, 45] Briefly, the total structure factor F is computed through a coherent addition of the bulk and surface contributions. The bulk structure is left unchanged while the surface structure is subject to change due to interfacial physiochemical processes including surface atom relaxation, foreign ion binding, and the adsorption of interfacial water. The displacement (dx, dy, dz) of each surface atom within an atomic layer was grouped according to the $\mathbf{b_s}$ glide plane symmetry mentioned above. Debye-Waller factors of surface atoms had negligible influence on the model fit (FOM), and thus they were fixed to bulk values. The refinement of surface atom occupancies is limited to the top three atom layers (Layer-1 O, Layer-2 O and Layer-3 Fe, Fig. S2), and the

partial occupancy of top three atom layers are constrained to be equivalent to account for the presence of FLT surface. Sorbate atoms (Sb atom and distal O atoms coordinating to Sb only) parameters include occupancy, Debye-Waller factor as well as positions. To reduce the number of free model parameters we applied geometrical constraints to maintain a near octahedral coordination shell of oxygen surrounding the Sb atom (details in the Supplementary Information), consistent with previous XAFS studies.[4, 17, 22] The occupancy of Sb and its coordinated distal O atoms are linked to be equivalent during model refinement. The distal O atoms are also constrained to have equivalent Debye-Waller factors. Interfacial water layers are included in the model by adding two pairs of O atoms above the substrate surface. The O atoms within each layer are grouped to have equivalent heights (z), occupancies, and Debye-Waller factors during model refinement. In addition, we applied $\mathbf{b_s}$ glide plane symmetry to constrain the in-plane positions of each O atom within the same water layer.

An additional constraint to the modeling included the use of bond-valence rules directly in the model refinement (detailed description in SI). In the process of model refinement, the bond valence saturation status of each surface atom is computed and used as a penalty factor *P*. Each structure model is fit against the CTR data to obtain the best fit model parameters including positions, Debye-Waller factors, and occupancies of surface and sorbate atoms, where the figure of merit (FOM) of the refinement includes both the comparison between experimental and calculated structure factors and the bond-valence penalty factor *P*. We applied a global optimization algorithm to minimize the figure of merit (FOM) during model refinement.[46, 47] The FOM is computed from the modified χ^2 value according to:

$$\mathrm{FOM} = P \sum_{i=1}^{N} \frac{\left[\frac{|F_i - F_{i,c}|}{e_i}\right]^2}{N-p}. \qquad (1)$$

In the equation (1), *P* is the bond valence penalty factor mentioned above, F_i represents the experimental value for the structure factor, $F_{i,c}$ is the calculated structure factor, e_i is the error of the i^{th} data point, *N* is the number of data points, and *p* is the number of fitting parameters.

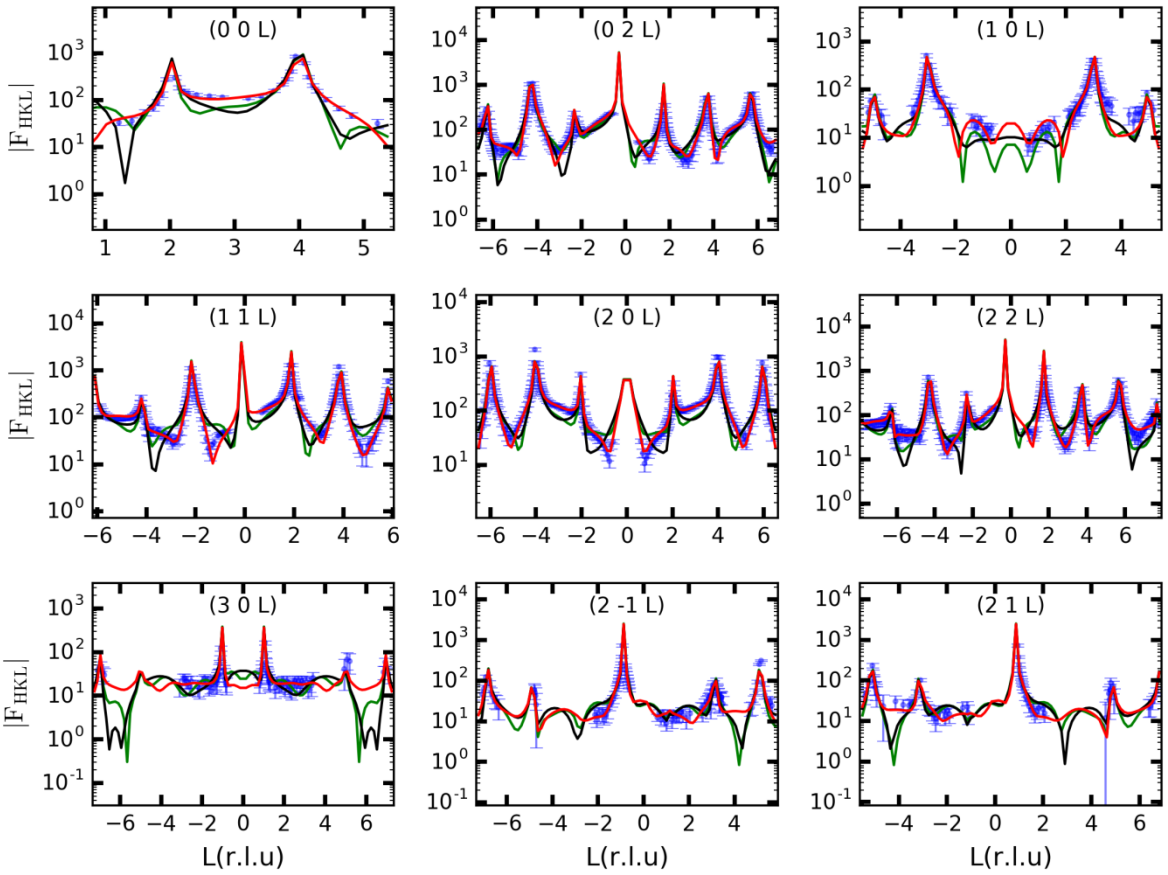

Figure 2. Experimental (blue circles) and model-based structure factors (F_{HKL}) as a function of perpendicular momentum transfer (L, in reciprocal lattice units) for the hematite ($1\bar{1}02$) surface reacted with 200 µM Sb(V) at pH 5.5. The green lines represent the calculated CTR profiles based on the optimized corner-sharing model (CS), black lines represent the calculated CTR profiles based on the optimized face-sharing model (FS), and red lines represent the calculated CTR profiles based on the optimized corner-sharing/edge-sharing model (CS&ES).

3. Results

3.1 Sb-bonded HLT

Optimized CTR profiles are compared to the experimental data in Fig. 2. Calculated CTRs based on Model CS (green lines in Fig. 2) and Model FS (black lines) could not reproduce the experimental data at numerous positions producing large FOM values (6.64 and 8.46 with bond-valence penalty factor *P* equaling 1, respectively). For example, sharp dips were observed near (1 1 -4), (1 1 2.5), and (2 2 -5.5) in the calculated profiles (Fig. 2). In addition, the valley features

observed at anti-Bragg peak regions near (2 0 L = ±1) could not be reproduced with those models. On the contrary, Model CS&ES yielded a significantly better fit to the experimental data with a FOM = 1.27 (bond-valence penalty factor *P*=1).

The best fit modeling results are compiled in Table S1. The best fit model gave rise to an average surface structure containing top three atom layers with partial occupancy of 0.79(3), which is equivalent to a 21(±3)% clean FLT surface and a 79(±3)% HLT surface. The HLT surface was partially occupied by Sb, where the occupancy of 0.37(2) corresponds to a coverage of 0.74(4) Sb/A_{UC} (A_{UC}= area of the unit cell, 27.4 Å²). The proportion of FLT to HLT was in good agreement with the ratio (72/28) previously reported on a clean surface [32] and a Pb(II)-reacted surface [48] using a similar preparation procedure. As shown in Fig. 3, the best fit structural model generated an Sb surface complex binding at the HLT surface in a tridentate mode with a corner-sharing/edge-sharing binding configuration. The Sb surface complex was slightly distorted from a regular octahedron with similar Sb-O bond lengths (3 × 2.11(3) Å, 2.03(3) Å, 2.07(3) Å and 2.09(5) Å) and a nearest Sb-Fe separation of 3.09(4) Å. It is worth noting the relatively large error of Debye-Waller factor parameter found for distal oxygen ligands (B = 2 (±4) Å^2). The large error bar is probably caused by the weak X-ray scattering for a distal oxygen ligand that undergoes fast exchange with free hydroxyl ions in solution. Additional model trials were performed to test the possible influence of this parameter on the surface binding structure. After a series of model refinements with the Debye-Waller factor for the distal oxygens fixed at three different values, i.e. 2, 4, and 6 Å^2, it was found that the results are comparable to the best-fit model within errors, suggesting negligible influence of these parameters.

3.2 Interfacial water structure

The best fit model also yielded an interfacial water structure that contained a near-surface water layer of an occupancy equivalent to ~1.0(2) O/A_{UC} at 3.2(1) Å above the surface and a second water layer with similar layer height (3.4(3) Å) and a smaller occupancy (0.4(2) O/A_{UC}). The heights of interfacial water layers observed in this work are much larger than those (1.19(7) Å and 1.91(4) Å) previously reported for a clean hydrated hematite surface ($1\bar{1}02$). [32] It appears that interfacial water molecules, pre-bound on the hematite surface, have been displaced by the Sb surface complex species. The interfacial waters observed here appear to be in positions

consistent with hydrogen bonding with the distal oxygen groups of the Sb surface complex rather than with surface oxygen groups, as shown in Fig. S3. The best fit model results suggest that the model fit quality (FOM) is insensitive to the Debye Waller factors of interfacial water layers. The variations of best fit Debye Waller factors within a relatively large value (5.4 and 20.0 $Å^2$ for the first and second water layer, respectively) only produce an increase of FOM smaller than 2%, which may hint at the weak lateral ordering of interfacial water layers above bound-Sb species on the hematite surface. We also found that model refinement using the structure model without interfacial water gave rise to a FOM = 1.52, a fit statistically worse, according to a Hamilton significance test on the ***R*** factor, [49] than the best fit using a structure model containing water layers (FOM = 1.27). Therefore, we conclude that interfacial water layers are probably displaced by the Sb surface complex that may form hydrogen-bonds with distal O ligands coordinating to Sb. The perturbation of the interfacial water structure induced by specific sorption of cations on a charged plate has been previously described in a molecular dynamics simulation study.[50] In that study, it was found that a localized point charge at a charged plate surface would compel and displace the interfacial water layer to larger distances from the substrate surface corresponding to so called 'translational ordering', similar to our findings here. Nonetheless, the interfacial water structure resolved in this work could not provide any insight into lateral structural ordering, likely due to a fast dynamic exchange between interfacial water molecules. Some water coverage closer to the surface, i.e. where no Sb occupies the surface, could also occur, but the low coverage and electron density (relative to the Sb surface complexes) means these water molecules do not contribute significantly to the scattering signal.

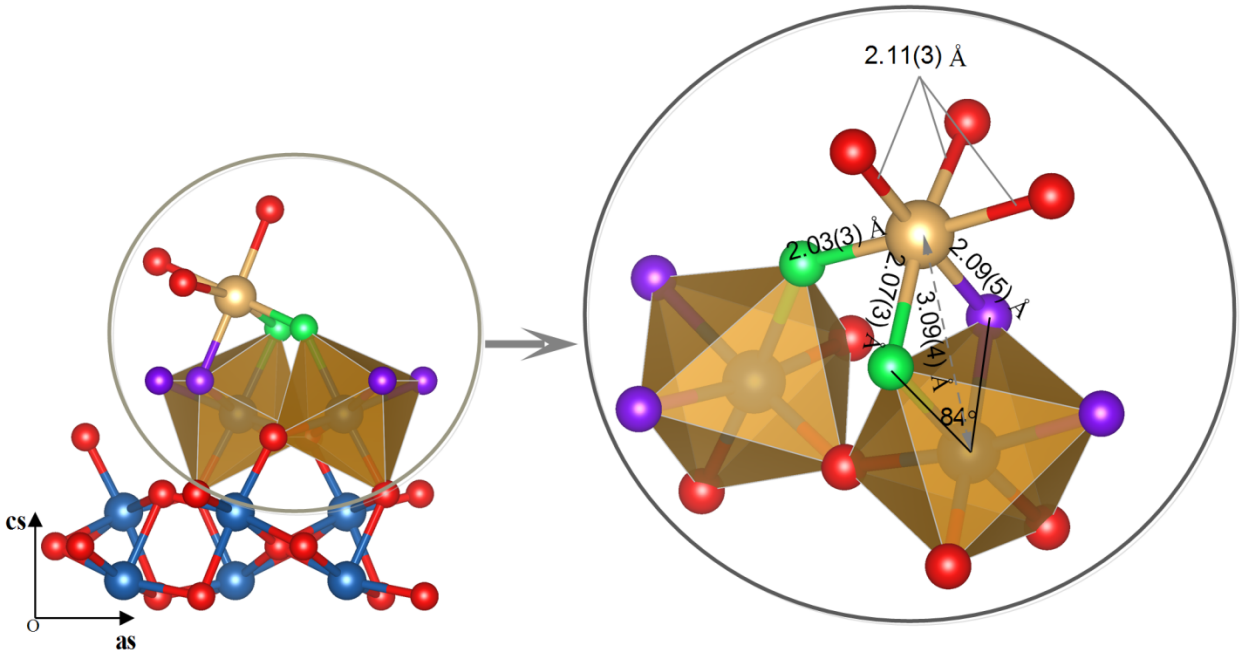

Figure 3. Left: A side view of molecular structure of the Sb(V) surface complex at the HLT of hematite ($1\bar{1}02$) surface based on the best fit Model CS&ES. Right: A detailed view of the Sb binding structure with proper orientation from the side view. The bond Sb-O lengths and the Sb-Fe separation are highlighted. The ^{I}O-Fe-^{II}O angle is also highlighted. Red spheres are O atoms, green spheres are singly coordinated surface O groups (^{I}O), purple spheres are doubly coordinated O groups (^{II}O), golden spheres are Sb atoms and blue spheres are Fe atoms. Near-surface Fe atoms are displayed as octahedra.

4. Discussion

4.1 Comparison of CTR-derived surface complexation structure with XAFS studies

The Sb surface complex species identified in this work has an nearest Sb-Fe separation (3.09(4) Å) as well as an average Sb-O bond length (2.14(5) Å) comparable to those reported in previous XAFS studies (3.00 to 3.19 Å for Sb-Fe distance, and 1.98(2) Å for Sb-O bond length) using differently synthesized substrates, including goethite,[17] ferrihydrite,[17] hydrous ferric oxide,[22] and environmental samples.[4, 26] In those XAFS studies, the Sb-Fe separations of 3.00-3.19 Å were assigned to Sb(V) adsorption in an edge-sharing mode. Besides the short Sb-Fe separation, a larger Sb-Fe separation (3.56 Å) is also found in shooting range soil samples,[4] and it was interpreted as corner-sharing surface complex species being simultaneously bound on the ferrihydrite surface. Our results suggest that the relatively short Sb-Fe distance is also consistent with the tridentate binding geometry, where the Sb complex shares both an edge and a corner of the Fe octahedra (Fig. 3). In addition, the best fit structure proposed in this work gives rise to a second nearest Sb-Fe distance (3.78 Å) that is much longer than the characteristic Sb-Fe distance (3.56 Å) found for a corner-sharing complexation structure. [4]

4.2 Implications of the mechanism controlling the surface binding mode

The binding mechanism of a specific ion on a mineral surface is determined by a variety of different factors. In the Sb-Fe (hydr)oxide systems the electrostatic repulsion between Sb(V) and Fe(III) was found to be an important factor that may regulate Sb uptake according to a DFT study.[23] This study suggests a general site preference trend with the larger Sb-Fe separation corresponding to the energetically more favorable binding structure due to weaker repulsion between the adsorbed Sb^{5+} cation and the nearest structural Fe^{3+} cation. The best fit model structure in this work suggests surface O atoms were displaced by up to 0.22 Å (Table S1). As a result, the ^{II}O-Fe-^{I}O bond angle (84(2)°, Fig. 3) shrinks significantly from the unrelaxed structure (^{II}O-Fe-^{I}O = 91°), while increasing the Fe-Sb distance. In the context of the electrostatic effects mentioned above, the reduction in the ^{II}O-Fe-^{I}O bond angle may be related to the necessity of maintaining a larger Sb-Fe separation to weaken the electrostatic repulsion. Further computational work could be helpful to disentangle the relationship between electrostatic repulsion and strain caused by structural distortion. The influence of electrostatic repulsion between the adsorbed and the structural cations was also highlighted in a study investigating the

effect of Sb(V) on the transformation of 2-line ferrihydrite to hematite, goethite and feroxyhyte.[51] In that study, it was found that the presence of Sb(V) favored the transformation of ferrihydrite to goethite and feroxyhyte while decreasing the yield of hematite. This phenomenon was interpreted as the consequence of the presence of face-sharing octahedral units in hematite structure, which inhibited the isomorphic substitution of Sb for Fe due to the strong Sb-Fe electrostatic repulsion.

However, electrostatic effects cannot be used to explain the binding preference of Sb at the tridentate ES_1&CS site compared to the bidentate CS site (Fig. 1) since Sb binding at the CS site would produce an even larger Sb-Fe separation (with weaker electrostatic repulsion) as described in previous XAFS studies.[3, 4, 22, 26] We propose the tridentate species described here is likely stabilized through a trade-off between the Sb-Fe repulsion and the energetic gains associated with the higher denticity, and relaxation of the surface. Such a tridentate binding configuration was not observed in the adsorption of another pentavalent ion As(V) on the same substrate surface.[43] Using X-ray reflectivity and Resonant Anomalous X-ray Reflectivity (RAXR), Catalano et al. find a binding structure of As(V), which consists of simultaneous inner-sphere and outer-sphere modes on hematite $(1\bar{1}02)$ surface.[43] The inner-sphere complex assumes a bidentate corner-sharing structure, which is similar to the CS site, one potential surface site we considered for Sb(V) binding as illustrated in Fig.1. The difference in binding configurations for these two pentavalent ions is probably driven by the size of the molecular ions. As shown above, the hematite surface needs to strain to accommodate $Sb(OH)_6^-$; the corresponding $H_2AsO_4^-$ unit has yet larger bond angles, which likely makes the trifold bonding to the surface thermodynamically unfavorable. In addition, the outer-sphere surface binding, deduced for As(V), is not observed for Sb(V) in this study. The simultaneous inner-sphere and outer-sphere binding modes was also reported for Pb(II) on hematite $(1\bar{1}02)$ surface in another RAXR study, [52] which was, however, not observed in our recent CTR work. [53] While the driving force of this simultaneous binding behavior remains unclear, the comparison of the binding structures between Sb(V) and As(V) on hematite $(1\bar{1}02)$ emphasize the importance of surface structure – reactivity relationship. Such a relationship should be addressed in a broader scope to take into considerations not only the substrate surface structure itself but also the coordination structure of sorbate ions.

4.3 Protonation schemes of interfacial oxygen groups

We predict the protonation schemes of surface functional groups in the best fit surface complex structure through a bond valence analysis, which was detailed in our group's recent publication.[48] With the protonation schemes of surface oxygen groups derived for this work (compiled in Table 1) and the associated protonation schemes for a clean hydroxylated surface reported previously,[32] we propose the surface reaction stoichiometry for Sb(V) adsorption as follows:

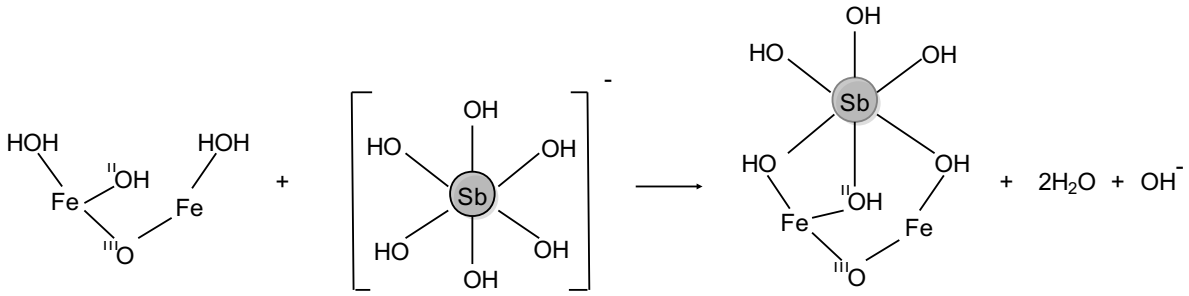

The stoichiometry outlined above indicates that surface complexation of Sb(V) on the HLT can be described as a ligand exchange between hydroxyl groups (-OH) coordinating to Sb and terminal hydro groups on the surface leading to the release of two water molecules and a hydroxide ion. In addition, Sb binding does not change the protonation state of the ^{II}O group but weakens the covalent hydrogen bond as suggested by a smaller bond valence of the H atom (0.68 v.u.) compared to that coordinating the unbound ^{II}O group (0.88 v.u.; Table 1). The release of one hydroxyl ion in the stoichiometry above implies that a lower solution pH will favor the uptake of Sb(V). This is consistent with the pH dependent sorption edge results reported previously using different types of Fe-(oxy)hydroxide samples,[12, 19, 25] which showed a maximum uptake at pH<7. It should be noted that the surface oxygen groups at a clean surface will protonate differently as a function of pH. For example, ^{I}O groups would deprotonate at a higher pH, which will change the reaction stoichiometry accordingly to produce two OH^- groups. Considering the relatively high pH (8-9) at the point of zero charge for hematite substrates,[36, 37] it is reasonable for the surface functional groups on the HLT to be fully protonated at pH 5.5 corresponding to one hydroxyl release in Sb surface complexation.

In light of the growing attention to the environmental risks associated with Sb contamination, especially at sites with potentially high Sb concentrations in soils and soil pore waters (e.g.

shooting ranges), the fundamental structural details presented in this study help to identify the potential species that would immobilize Sb(V) through surface complexation reactions with iron-(hydr)oxides. The surface complexation reaction proposed in this work also predicts that Sb(V) uptake will be more effective under acidic conditions.

5. Environmental impact

Our results improve the molecular level understanding of the retention of Sb(V), an emerging contaminant in the environment, by Fe-bearing mineral phases. The proposed three-fold coordinated IS binding mode suggests a strong interaction with the mineral phase, which may indicate low mobility of Sb(V) under the experimental conditions of our work, and the possibility for remediation processes based on this molecular process. One aspect of this is the absence of a co-existing OS species, which had been previously observed for the adsorption of As(V) on the same hematite $(1\bar{1}02)$ surface.

The molecular scale binding structure derived in this CTR work has its limitation in a single set of reaction conditions, but it will nonetheless serve as a molecular reference in future research for example with respect to thermodynamic surface complexation modelling, chemically-guided reactive transport simulations, or quantum chemical studies to elucidate energetic barriers in the adsorption processes of molecular anion contaminants.

Table 1. Bond valence analysis of surface species based on the best fit structure model.

Surface Species	Original bond valence sum (v.u)	Protonation scheme and hydrogen bonding		Final bond valence sum (v.u)
		Number of H	Number of H bond	
Fe≡**O**—Sb	1.24	1 (0.76)	0	2.00
Fe≡**O**—Sb	1.13	1 (0.87)	0	2.00
Fe_2≡**O**—Sb	1.44	1 (0.68)	0	2.12
Fe_2≡**O**	0.70	1 (0.88)	1 (0.25)	1.83
Fe_3≡**O**	1.87	0	1 (0.13)	2.00
$\mathbf{O}_{dist}$—Sb	0.68	1(0.88)	2 (0.22)	2.00

The numbers inside the parentheses are bond valence sums assigned to a covalent hydrogen (H) or a hydrogen bond (H bond), so that a bond valence sum is closest to the saturation state. The ranges of the valence for an H and an H bond are 0.68-0.88 v.u and 0.13-0.25 v.u, respectively as suggested by Bargar et al.[54]

Supporting information: CTR model refinement strategy, bond valence constraint, geometrical solution in model refinement (Figure S1), structure comparison between two surface terminations of hematite ($1\bar{1}02$) (Figure S2), interfacial water structure (Figure S3), table of best fit CTR model (Table S1)

Acknowledgements

This project was funded by the Department of Defense's Strategic Environmental Research and Development Program under grant ER-1770. All the experiments were performed at beamline 13BMC of GeoSoilEnviroCARS (Sector 13), Advanced Photon Source (APS), Argonne National Laboratory. GSECARS is supported by the National Science Foundation - Earth Sciences (EAR-1128799 and EAR-1634415) and the Department of Energy - Geosciences (DE-FG02-94ER14466). Use of the Advanced Photon Source was supported by the U. S. Department of Energy, Office of Science, Office of Basic Energy Sciences, under Contract No. DE-AC02-06CH11357. Part of this work was co-financed by the Helmholtz Gemeinschaft Deutscher Forschungszentren by supporting the Helmholtz-Nachwuchsgruppe "Structures and Reactivity at the Water/Mineral Interface" (VH-NG-942). We thank Joanne Stubbs and Peter Eng from GSECARS beamline at APS for great help with data collection as well as constructive discussions on this manuscript. We would also like to thank the Arctic Super Computer Center (ARSC) at the University of Alaska Fairbanks for providing computational resources used in the surface structure fitting.

References

1. Filella, M.; Belzile, N.; Chen, Y.-W., Antimony in the environment: a review focused on natural waters: I. Occurrence. *Earth-Science Reviews* **2002,** *57*, (1), 125-176.

2. Wilson, S. C.; Lockwood, P. V.; Ashley, P. M.; Tighe, M., The chemistry and behaviour of antimony in the soil environment with comparisons to arsenic: a critical review. *Environmental Pollution* **2010,** *158*, (5), 1169-1181.
3. Ackermann, S.; Gieré, R.; Newville, M.; Majzlan, J., Antimony sinks in the weathering crust of bullets from Swiss shooting ranges. *Science of the Total Environment* **2009,** *407*, (5), 1669-1682.
4. Scheinost, A. C.; Rossberg, A.; Vantelon, D.; Xifra, I.; Kretzschmar, R.; Leuz, A.-K.; Funke, H.; Johnson, C. A., Quantitative antimony speciation in shooting-range soils by EXAFS spectroscopy. *Geochimica et Cosmochimica Acta* **2006,** *70*, (13), 3299-3312.
5. Sundar, S.; Chakravarty, J., Antimony toxicity. *International journal of environmental research and public health* **2010,** *7*, (12), 4267-4277.
6. IARC, Some organic solvents, resin monomers and related compounds, pigments and occupational exposures in paint manufacture and painting. *IARC Monogr. Eval. Carcinog. risks to humans* **1990,** *47*.
7. Rawcliffe, C., Antimony in medical history. In British Medical Journal Publishing Group: 2000; Vol. 320, p 879.
8. Herwaldt, B. L.; Berman, J. D., Recommendations for treating leishmaniasis with sodium stibogluconate (Pentostam) and review of pertinent clinical studies. *The American journal of tropical medicine and hygiene* **1992,** *46*, (3), 296-306.
9. Franco, M. A.; Barbosa, A. C.; Rath, S.; Dorea, J. G., Antimony oxidation states in antileishmanial drugs. *The American journal of tropical medicine and hygiene* **1995,** *52*, (5), 435-437.
10. US EPA, List of drinking water contaminants and their maximum contaminant levels. **2009**.
11. Ilgen, A. G.; Majs, F.; Barker, A.; Douglas, T.; Trainor, T., Oxidation and mobilization of metallic antimony in aqueous systems with simulated groundwater. *Geochimica et Cosmochimica Acta* **2014,** *132*, 16-30.
12. Leuz, A.-K.; Mönch, H.; Johnson, C. A., Sorption of Sb (III) and Sb (V) to goethite: influence on Sb (III) oxidation and mobilization. *Environmental science & technology* **2006,** *40*, (23), 7277-7282.
13. Xi, J.; He, M.; Wang, K.; Zhang, G., Adsorption of antimony (III) on goethite in the presence of competitive anions. *Journal of Geochemical Exploration* **2013,** *132*, 201-208.
14. Kong, L.; Hu, X.; He, M., Mechanisms of Sb (III) oxidation by pyrite-induced hydroxyl radicals and hydrogen peroxide. *Environmental science & technology* **2015,** *49*, (6), 3499-3505.
15. Mitsunobu, S.; Takahashi, Y.; Terada, Y., μ-XANES evidence for the reduction of Sb (V) to Sb (III) in soil from Sb mine tailing. *Environmental science & technology* **2010,** *44*, (4), 1281-1287.
16. Filella, M.; Belzile, N.; Chen, Y.-W., Antimony in the environment: a review focused on natural waters: II. Relevant solution chemistry. *Earth-Science Reviews* **2002,** *59*, (1), 265-285.
17. Mitsunobu, S.; Takahashi, Y.; Terada, Y.; Sakata, M., Antimony (V) incorporation into synthetic ferrihydrite, goethite, and natural iron oxyhydroxides. *Environmental Science & Technology* **2010,** *44*, (10), 3712-3718.
18. Resongles, E.; Casiot, C.; Elbaz-Poulichet, F.; Freydier, R.; Bruneel, O.; Piot, C.; Delpoux, S.; Volant, A.; Desoeuvre, A., Fate of Sb (V) and Sb (III) species along a gradient of pH and oxygen concentration in the Carnoules mine waters (Southern France). *Environmental Science: Processes & Impacts* **2013,** *15*, (8), 1536-1544.

19. Martínez-Lladó, X.; de Pablo, J.; Giménez, J.; Ayora, C.; Marti, V.; Rovira, M., Sorption of antimony (V) onto synthetic goethite in carbonate medium. *Solvent Extraction and Ion Exchange* **2008,** *26*, (3), 289-300.
20. Cai, Y.; Li, L.; Zhang, H., Kinetic modeling of pH-dependent antimony (V) sorption and transport in iron oxide-coated sand. *Chemosphere* **2015,** *138*, 758-764.
21. Ilgen, A. G.; Trainor, T. P., Sb (III) and Sb (V) sorption onto Al-rich phases: hydrous Al oxide and the clay minerals kaolinite KGa-1b and oxidized and reduced nontronite NAu-1. *Environmental science & technology* **2011,** *46*, (2), 843-851.
22. Guo, X.; Wu, Z.; He, M.; Meng, X.; Jin, X.; Qiu, N.; Zhang, J., Adsorption of antimony onto iron oxyhydroxides: adsorption behavior and surface structure. *Journal of hazardous materials* **2014,** *276*, 339-345.
23. Mason, S. E.; Trainor, T. P.; Goffinet, C. J., DFT study of Sb (III) and Sb (V) adsorption and heterogeneous oxidation on hydrated oxide surfaces. *Computational and Theoretical Chemistry* **2012,** *987*, 103-114.
24. Ramadugu, S. K.; Mason, S. E., DFT Study of Antimony (V) Oxyanion Adsorption on α-Al2O3 (1$\bar{1}$02). *The Journal of Physical Chemistry C* **2015,** *119*, (32), 18149-18159.
25. Vithanage, M.; Rajapaksha, A. U.; Dou, X.; Bolan, N. S.; Yang, J. E.; Ok, Y. S., Surface complexation modeling and spectroscopic evidence of antimony adsorption on iron-oxide-rich red earth soils. *Journal of colloid and interface science* **2013,** *406*, 217-224.
26. Ritchie, V. J.; Ilgen, A. G.; Mueller, S. H.; Trainor, T. P.; Goldfarb, R. J., Mobility and chemical fate of antimony and arsenic in historic mining environments of the Kantishna Hills district, Denali National Park and Preserve, Alaska. *Chemical Geology* **2013,** *335*, 172-188.
27. McComb, K. A.; Craw, D.; McQuillan, A. J., ATR-IR spectroscopic study of antimonate adsorption to iron oxide. *Langmuir* **2007,** *23*, (24), 12125-12130.
28. Koningsberger, D.; Prins, R., X-ray absorption: principles, applications, techniques of EXAFS, SEXAFS, and XANES. **1988**.
29. Brown Jr, G.; Parks, G.; O'day, P., Sorption at mineral-water interfaces: macroscopic and microscopic perspectives. *Mineral surfaces* **1995,** *5*, 129-183.
30. Robinson, I. K., Crystal truncation rods and surface roughness. *Physical Review B* **1986,** *33*, (6), 3830.
31. Catalano, J. G.; Fenter, P.; Park, C., Interfacial water structure on the (012) surface of hematite: ordering and reactivity in comparison with corundum. *Geochimica et Cosmochimica Acta* **2007,** *71*, (22), 5313-5324.
32. Tanwar, K. S.; Lo, C. S.; Eng, P. J.; Catalano, J. G.; Walko, D. A.; Brown, G. E.; Waychunas, G. A.; Chaka, A. M.; Trainor, T. P., Surface diffraction study of the hydrated hematite surface. *Surface Science* **2007,** *601*, (2), 460-474.
33. Lo, C. S.; Tanwar, K. S.; Chaka, A. M.; Trainor, T. P., Density functional theory study of the clean and hydrated hematite (1 1$\bar{}$ 02) surfaces. *Physical review B* **2007,** *75*, (7), 075425.
34. Tanwar, K. S.; Catalano, J. G.; Petitto, S. C.; Ghose, S. K.; Eng, P. J.; Trainor, T. P., Hydrated α-Fe 2 O 3 surface structure: Role of surface preparation. *Surface science* **2007,** *601*, (12), L59-L64.
35. McBriarty, M. E.; von Rudorff, G. F.; Stubbs, J. E.; Eng, P. J.; Blumberger, J.; Rosso, K. M., Dynamic Stabilization of Metal Oxide–Water Interfaces. *Journal of the American Chemical Society* **2017,** *139*, (7), 2581-2584.
36. Kosmulski, M., The pH-dependent surface charging and points of zero charge: V. Update. *Journal of colloid and interface science* **2011,** *353*, (1), 1-15.

37. Kallay, N.; Preočanin, T., Measurement of the surface potential of individual crystal planes of hematite. *Journal of Colloid and Interface Science* **2008,** *318*, (2), 290-295.
38. Trainor, T. P.; Eng, P. J.; Robinson, I. K., Calculation of crystal truncation rod structure factors for arbitrary rational surface terminations. *Journal of applied crystallography* **2002,** *35*, (6), 696-701.
39. You, H., Angle calculations for a4S+ 2D'six-circle diffractometer. *Journal of applied crystallography* **1999,** *32*, (4), 614-623.
40. Eikenberry, E.; Brönnimann, C.; Hülsen, G.; Toyokawa, H.; Horisberger, R.; Schmitt, B.; Schulze-Briese, C.; Tomizaki, T., PILATUS: a two-dimensional X-ray detector for macromolecular crystallography. *Nuclear Instruments and Methods in Physics Research Section A: Accelerators, Spectrometers, Detectors and Associated Equipment* **2003,** *501*, (1), 260-266.
41. Schlepütz, C.; Herger, R.; Willmott, P.; Patterson, B.; Bunk, O.; Brönnimann, C.; Henrich, B.; Hülsen, G.; Eikenberry, E., Improved data acquisition in grazing-incidence X-ray scattering experiments using a pixel detector. *Acta Crystallographica Section A: Foundations of Crystallography* **2005,** *61*, (4), 418-425.
42. Finger, L. W.; Hazen, R. M., Crystal structure and isothermal compression of Fe_2O_3, Cr_2O_3, and V_2O_3 to 50 kbars. *Journal of Applied Physics* **1980,** *51*, (10), 5362-5367.
43. Catalano, J. G.; Park, C.; Fenter, P.; Zhang, Z., Simultaneous inner- and outer-sphere arsenate adsorption on corundum and hematite. *Geochimica et Cosmochimica Acta* **2008,** *72*, (8), 1986-2004.
44. Vlieg, E., ROD: a program for surface X-ray crystallography. *Journal of Applied Crystallography* **2000,** *33*, (2), 401-405.
45. Fenter, P. A., X-ray reflectivity as a probe of mineral-fluid interfaces: A user guide. *Reviews in mineralogy and geochemistry* **2002,** *49*, (1), 149-221.
46. Björck, M., Fitting with differential evolution: an introduction and evaluation. *Journal of Applied Crystallography* **2011,** *44*, (6), 1198-1204.
47. Björck, M.; Andersson, G., GenX: an extensible X-ray reflectivity refinement program utilizing differential evolution. *Journal of Applied Crystallography* **2007,** *40*, (6), 1174-1178.
48. Qiu, C.; Majs, F.; Eng, P. J.; Stubbs, J. E.; Douglas, T. A.; Schmidt, M.; Trainor, T. P., In situ structural study of the surface complexation of lead (II) on the chemically mechanically polished hematite ($11\bar{2}0$) surface. *Journal of colloid and interface science* **2018,** *524*, 65-75.
49. Hamilton, W. C., Significance tests on the crystallographic R factor. *Acta Crystallographica* **1965,** *18*, (3), 502-510.
50. Dewan, S.; Carnevale, V.; Bankura, A.; Eftekhari-Bafrooei, A.; Fiorin, G.; Klein, M. L.; Borguet, E., Structure of Water at Charged Interfaces: A Molecular Dynamics Study. *Langmuir* **2014,** *30*, (27), 8056-8065.
51. Michael Bolanz, R.; Bläss, U.; Ackermann, S.; Ciobotă, V.; Rösch, P.; Tarcea, N.; Popp, J.; Majzlan, J., The effect of antimonate, arsenate, and phosphate on the transformation of ferrihydrite to goethite, hematite, feroxyhyte, and tripuhyite. *Clays and Clay Minerals* **2013,** *61*, (1), 11-25.
52. Noerpel, M. R.; Lee, S. S.; Lenhart, J. J., X-ray Analyses of Lead Adsorption on the (001),(110), and (012) Hematite Surfaces. *Environmental science & technology* **2016,** *50*, (22), 12283-12291.
53. Qiu, C.; Majs, F.; Eng, P. J.; Stubbs, J. E.; Douglas, T. A.; Schmidt, M.; Trainor, T. P., In situ structural study of the surface complexation of lead(II) on the chemically mechanically polished hematite (1-102) surface. *Journal of Colloid and Interface Science* **2018,** *524*, 65-75.

54. Bargar, J.; Brown, G.; Parks, G., Surface complexation of Pb (II) at oxide-water interfaces: II. XAFS and bond-valence determination of mononuclear Pb (II) sorption products and surface functional groups on iron oxides. *Geochimica et Cosmochimica Acta* **1997,** *61*, (13), 2639-2652.